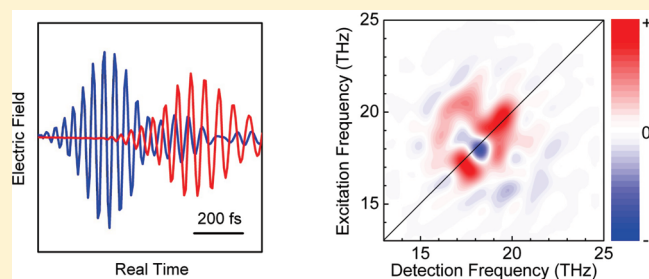


Two-Dimensional Terahertz Correlation Spectra of Electronic Excitations in Semiconductor Quantum Wells

W. Kuehn,[†] K. Reimann,[†] M. Woerner,^{*,†} T. Elsaesser,[†] and R. Hey[‡][†]Max-Born-Institut für Nichtlineare Optik und Kurzzeitspektroskopie, 12489 Berlin, Germany[‡]Paul-Drude-Institut für Festkörperelektronik, 10117 Berlin, Germany

ABSTRACT: We discuss a novel approach for nonlinear two-dimensional (2D) spectroscopy in the terahertz (THz) frequency range which is based on a collinear interaction geometry of a sequence of THz pulses with the sample. The nonlinear polarization is determined by a phase-resolved measurement of the electric field transmitted through the sample as a function of the delay τ between two phase-locked pulses and the “real” time t . The information provided by a single 2D scan along the τ and t axes is equivalent to that from a noncollinear photon-echo setup equipped with four local oscillators, each interacting with a different diffracted order. We address basic concepts of collinear 2D THz spectroscopy, in particular data analysis and phasing issues. Different rephasing and nonrephasing contributions to the third-order response are separated and 2D correlation spectra derived. As a prototype application, 2D correlation spectra of intersubband excitations of electrons in semiconductor quantum wells are presented.



1. INTRODUCTION

Two-dimensional (2D) spectroscopy in the femtosecond time domain has developed into an important method to unravel the dynamics of electronic and/or vibrational excitations of matter and, in particular, to determine the couplings between different excitations.^{1–10} 2D spectroscopy in the visible and ultraviolet ranges has provided insight into solvation dynamics of individual molecular chromophores,¹¹ excitonic couplings and excitation transfer in molecular aggregates,¹² nanotubes,¹³ and macromolecular light harvesting systems^{14–16} and into the nonlinear response of excitons in bulk and low-dimensional semiconductors.^{17–19} In molecular systems, vibrational dynamics and interactions, chemical processes, and, to some extent, structure and structural fluctuations have been mapped by 2D spectroscopy in the infrared wavelength range between 2.5 and 7 μm .^{2,3,5,9,10,20–28}

Most 2D studies have addressed the third-order ($\chi^{(3)}$) nonlinear response of the system under study. A variety of pump–probe and photon-echo techniques have been applied to determine third-order signals as a function of two frequencies, the excitation frequency ν_1 and the detection frequency ν_3 .²⁹ In the widely applied four-wave mixing or photon-echo method, three ultrashort pulses with noncollinear propagation directions \mathbf{k}_1 , \mathbf{k}_2 , and \mathbf{k}_3 interact with the sample, and the diffracted photon-echo signal is heterodyne detected by interferometry with a fourth pulse, the local oscillator.^{3,7} The pulse sequence used in such measurements is shown schematically in Figure 1. Photon-echo signals are measured as a function of the coherence or excitation time τ_{ex} , the delay between pulse 1 and 2, the waiting or population time T_{W} , the delay between pulse 2 and 3, and the detection time t_{det} after the signal generation by pulse 3. A double

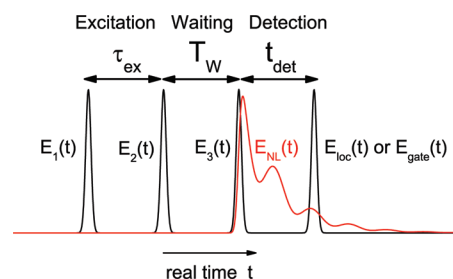


Figure 1. Timing sequence of three interactions of the investigated system with driving fields $E_1(t)$, $E_2(t)$, and $E_3(t)$ and the electric field emitted by third-order nonlinear polarization $E_{\text{NL}}(t)$. Phase-resolved detection of the latter is realized either by interference with a local oscillator pulse $E_{\text{loc}}(t)$ or in direct field-resolved detection using electro-optic sampling by a gate pulse $E_{\text{gate}}(t)$. The periods between the respective pulses are identified as the excitation period τ_{ex} , waiting period T_{W} , and detection period t_{det} of the nonlinear response function.

Fourier transform of the time-domain signal along τ_{ex} and t_{det} provides the frequency axis $\nu_{\tau_{\text{ex}}} = \nu_1$ and $\nu_{t_{\text{det}}} = \nu_3$. The time evolution of the signal during the period T_{W} reflects spectral diffusion processes, fluctuating couplings, and/or relaxation processes or even the time evolution of Raman coherences.³⁰ The theoretical analysis of 2D spectra is mainly based on third-order

Special Issue: Shaul Mukamel Festschrift

Received: October 15, 2010

Revised: November 5, 2010

Published: December 20, 2010

Table 1. Time Ordering and Frequency Vectors $\vec{\nu} = (\nu_b, \nu_\tau)$ of Six Different Contributions to the Third-Order Nonlinear Signal Shown in Figure 3^a

experiment	delay	ν_t	ν_τ	τ_{ex}	T_W	t_{det}
(a) A–B–B photon echo	$\tau < 0$	$2\nu_B - \nu_A$	ν_A	$-\tau$	$T = 0$	t
(b) A pump–B probe	$\tau < 0$	ν_B	0	$T = 0$	$-\tau$	t
(c) PFID A pump–B probe	$\tau > 0$	ν_B	0	τ	$T = 0$	$t - \tau$
(d) B pump–A probe	$\tau > 0$	ν_A	$-\nu_A$	$T = 0$	τ	$t - \tau$
(e) PFID B pump–A probe	$\tau < 0$	ν_A	$-\nu_A$	$-\tau$	$T = 0$	t
(f) B–A–A photon echo	$\tau > 0$	$2\nu_A - \nu_B$	$-2\nu_A$	τ	$T = 0$	$t - \tau$

^a Columns 5–7 explain the respective relations to the excitation period τ_{ex} , waiting period T_W , and detection period t_{det} shown in Figure 1.

response functions calculated in a perturbative density matrix approach and double-sided Feynman diagrams visualizing the different Liouville-space pathways that contribute to the measured third-order signal.¹ While most experiments on vibrational excitations are safely in the third-order limit, higher-order contributions have been identified in the nonlinear electronic response of model systems such as excitons or intersubband excitations in semiconductors.^{18,19,31,32}

Recently, we have introduced a novel technique of 2D spectroscopy in the terahertz (THz) frequency range which is based on a collinear interaction geometry (in combination with phase cycling, such a geometry was used in ref 31) of the pulses with the sample and a phase-resolved detection of the transmitted light with the help of electro-optic sampling.³² This method is close to concepts of multidimensional nuclear magnetic resonance (NMR),³³ and THz pulse areas of up to several π are readily implemented in this scheme. We have demonstrated the potential of this method by decomposing resonant nonlinear intersubband excitations in GaAs/AlGaAs quantum wells into different nonlinearities $\chi^{(n)}$ with $n \geq 3$. Since the phase, amplitude, and frequency of each relevant pulse are measured directly, additional phasing procedures known from noncollinear 2D photon-echo experiments are avoided.^{34,35} The real part and the imaginary part of the spectrum are determined without any additional experiment.

In this article, we report—in extension of this work—2D THz correlation spectra determined by this method. We study intersubband transitions in semiconductor quantum wells³⁶ and demonstrate that a single 2D scan provides the full information about four-wave mixing and pump–probe contributions at the same time. Each contribution can be analyzed individually in the frequency domain. Moreover, the 2D Fourier transformation improves the signal-to-noise ratio drastically, as signal and noise are decoupled along two time axes. In the following, we first introduce the method and discuss 2D correlation spectra and phasing issues (section 2). In section 3, we present the experimental results together with an analysis of the underlying intersubband excitations. Conclusions are given in section 4.

2. METHOD

2.1. Rephasing and Nonrephasing Nonlinear Signals. The concept of collinear 2D spectroscopy in the THz range has been presented in ref 32. In the following, we recall some basic principles and discuss rephasing and nonrephasing contributions to the third-order response measured in a collinear geometry. To allow for a direct comparison with work on a noncollinear photon-echo geometry,⁷ we consider a sequence of three identical pulses interacting with the sample.

In collinear 2D THz spectroscopy, phase-locked pulses A, B, and C with a carrier frequency ν_0 are generated by nonlinear

frequency conversion, e.g., by parametric difference frequency mixing driven by the output of a femtosecond laser.³⁷ Choppers in each beam synchronized with the laser repetition rate allow for sending single pulses A, B, or C, phase-locked pulse pairs AB, BC, or CA, or all pulses ABC (Figure 1) onto the sample. After interaction with the sample, the transmitted electric field is measured in real time t by electro-optic sampling where the fourth pulse serves as the gating pulse. In this way, one obtains the electric field transients of all possible combinations, i.e., $E_A(t, T, \tau)$, $E_B(t, T)$, $E_C(t)$, $E_{AB}(t, T, \tau)$, ..., $E_{ABC}(t, T, \tau)$. Such signals contain the fields emitted by nonlinear polarizations of arbitrary order and the transmitted pulses. In typical measurements, the delay τ between pulses A and B is varied, while the delay T between pulses B and C remains fixed. The third-order nonlinear response of the sample is derived from

$$E_{\text{NL}}(t, T, \tau) = E_{\text{ABC}}(t, T, \tau) - E_{\text{AB}}(t, T, \tau) - E_{\text{BC}}(t, T) - E_{\text{CA}}(t, T, \tau) + E_A(t, T, \tau) + E_B(t, T) + E_C(t) \quad (1)$$

A two-dimensional Fourier transform of $E_{\text{NL}}(t, T, \tau)$ along the two time variables t and τ gives $F_{\text{NL}}(\nu_b, \nu_\tau)$, the nonlinear signal in 2D frequency space. In the collinear experimental scheme, the 2D frequency space has a one-to-one correspondence with the wave-vector space used in a noncollinear geometry of interaction.³² The electric field of pulses A, B, and C can be written as a product of a slowly varying envelope and a carrier wave with frequency ν_0

$$\begin{aligned} E_A(t, T, \tau) &= \frac{\varepsilon_A(t + T - \tau)}{2} \exp\{-i2\pi\nu_0(t + T - \tau)\} + c.c. \\ E_B(t, T) &= \frac{\varepsilon_B(t + T)}{2} \exp\{-i2\pi\nu_0(t + T)\} + c.c. \\ E_C(t) &= \frac{\varepsilon_C(t)}{2} \exp\{-i2\pi\nu_0 t\} + c.c. \end{aligned} \quad (2)$$

The experimental parameters (times) t and τ play a 2-fold role in the analysis presented in the following. They (i) serve as an identification of the respective electric field (eq 2) in the applied pulse sequence along the path in Liouville space and (ii) represent one of the periods in the nonlinear response function, i.e., either the excitation period τ_{ex} , waiting period T_W , or detection period t_{det} depending on the respective time ordering of pulses A, B, and C (cf. discussion of Table 1 and Figure 3 below).

The experimental parameters t and τ are the Fourier conjugates of a two-dimensional frequency vector $\vec{\nu} = (\nu_b, \nu_\tau)$ which

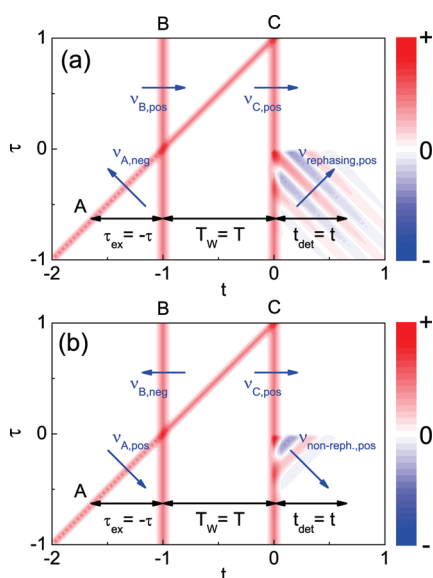


Figure 2. Two-dimensional contour plots of three Gaussian electric field pulses A, B, and C as a function of both the real time t and the delay τ between pulses A and B. The delay $T = T_W$ between pulses B and C is a fixed parameter in this plot. (a) The electric field of the photon echo (rephasing contribution to the nonlinear signal) occurs in the quadrant with $t > 0$ and $\tau < 0$ with phase fronts perpendicular to those of pulse A. (b) Corresponding nonrephasing signal identified by phase fronts parallel to that of pulse A. The orientation of the phase fronts in the two-dimensional time domain (t and τ) can be determined uniquely by the orientation of the respective frequency vector $\vec{\nu}$ (blue arrows) in the two-dimensional Fourier domain (ν_t and ν_τ).

replaces the \mathbf{k} -vectors used in the phase-matching geometries of noncollinear photon-echo spectroscopy.⁷ The two-dimensional Fourier transform $F(\nu_t, \nu_\tau)$ of any electric field $E(t, T, \tau)$ allows for uniquely identifying the orientation of its phase fronts in the time domain with the help of the two-dimensional frequency vector $\vec{\nu} = (\nu_t, \nu_\tau)$ of its carrier wave. The blue arrows in Figure 2 which are perpendicular to the phase fronts of the respective pulses A, B, and C (red contours) indicate the direction of $\vec{\nu}$. The index pos and neg stands for the positive and negative frequency component of the electric fields in eq 2, respectively. The scheme shown in the upper panel of Figure 2 represents the rephasing contribution to the third-order photon echo according to

$$P_{\text{FWM}}^{(3)}(t, \tau) \propto E_A^*(t + T - \tau) E_B(t + T) E_C(t) \exp[-i2\pi\nu_0 t] \exp[-i2\pi\nu_0 \tau] \quad (3)$$

which includes the set of double-sided Feynman diagrams plotted in the upper-most panel of Figure 5 of ref 7. An advantage of the frequency vector representation is that one can visualize the different Liouville pathways which contribute to a nonlinear polarization of n th order as a chain of arrows indicating the interaction with various contributions to the electric field (see also Figure 1 of ref 32). In Figure 2(a), the electric field of the photon echo (rephasing contribution) occurs in the quadrant with $t > 0$ ($t_{\text{det}} > 0$) and $\tau < 0$ ($\tau_{\text{ex}} > 0$) with phase fronts perpendicular to those of pulse A. The corresponding chain of frequency vectors $E_A^{\text{neg}} \rightarrow E_B^{\text{pos}} \rightarrow E_C^{\text{pos}}$ leads to a nonlinear polarization emitting an electric field with the carrier wave $\exp\{-i2\pi\nu_0(t + \tau)\} = \exp\{-i2\pi\nu_0(t_{\text{det}} - \tau_{\text{ex}})\}$ with an obviously rephasing character.

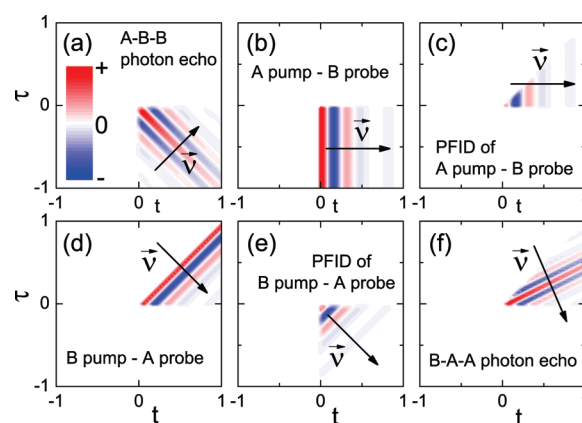


Figure 3. Contributions to the third-order nonlinear signal measured simultaneously in our collinear beam geometry. The panels show the result of model calculations for an inhomogeneous ensemble of two-level systems driven by two δ -like pulses A and B. The six contour plots show the nonlinearly emitted electric field as a function of t and τ . The black arrows indicate the frequency vectors $\vec{\nu}$ discussed in the main text. PFID stands for perturbed free induction decay.

The nonrephasing contribution to the third-order response is illustrated in Figure 2(b). Here, the nonrephasing signal is characterized by phase fronts parallel to those of pulse A. The interaction sequence $E_A^{\text{pos}} \rightarrow E_B^{\text{neg}} \rightarrow E_C^{\text{pos}}$ leads to a nonlinear polarization emitting an electric field with the carrier wave $\exp\{-i2\pi\nu_0(t - \tau)\} = \exp\{-i2\pi\nu_0(t_{\text{det}} + \tau_{\text{ex}})\}$ showing a nonrephasing character. In collinear 2D spectroscopy, the rephasing and nonrephasing signal are obtained in an identical pulse sequence A–B–C but differ in the direction of the frequency vector $\vec{\nu}$. In contrast, in a noncollinear three-pulse photon-echo setup,⁷ the two signals are observed in an identical diffraction direction but differ in the time ordering of the pulses.

The two-dimensional time domain representation of the nonlinear signals in Figure 2 gives an intuitive explanation for the fact that the separate rephasing and nonrephasing contributions give “phase twisted 2D spectra”.⁷ Causality restricts the nonlinear signal to the quadrant with $t > 0$ ($t_{\text{det}} > 0$) and $\tau < 0$ ($\tau_{\text{ex}} > 0$). After a two-dimensional Fourier transform, the sharp corner of this quadrant causes a complex mixing of the dispersive and absorptive parts of the line shape, i.e., rephasing or nonrephasing phase twisted 2D spectra.

In the following, we focus on the case of a vanishing waiting (population) time $T_W = T = 0$. This limit is equivalent to a two-pulse experiment (pulses B and C are identical) generating a third-order signal given by

$$E_{\text{NL}}(t, \tau) = E_{\text{AB}}(t, \tau) - E_A(t, \tau) - E_B(t) \quad (4)$$

2.2. Two-Dimensional Correlation Spectra and Phasing.

In the collinear interaction geometry, the nonlinear polarization measured in a single 2D scan along the t and τ axes (cf. Figure 6) provides the accumulated information that could be gained in a noncollinear photon-echo setup (e.g., Figure 9 of ref 7) by implementing a total of four local oscillators, each positioned at the output beam of a different diffracted order. In other words, the six different experiments visualized and analyzed in Figure 3 and Table 1 are performed simultaneously in the collinear case. Furthermore, the different nonlinear signals are measured in definite phase relation to each other. Thus, the correct interference

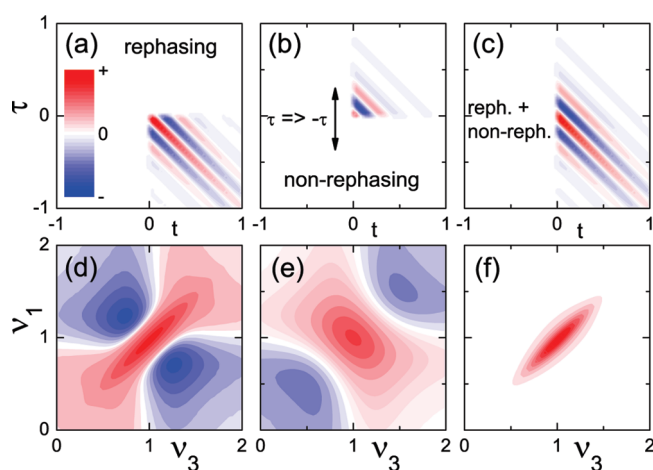


Figure 4. Making of a 2D IR correlation spectrum with purely absorptive line shapes ($T = T_W = 0$). (a) Rephasing contribution: A–B–B photon echo of Figure 3. (b) Corresponding nonrephasing contribution: ($\tau \leftrightarrow -\tau$)-inverted perturbed free induction decay of B pump–A probe experiment [Figure 3(e)]. (c) Sum of the rephasing and non-rephasing contribution. Lower row: the corresponding 2D correlation spectra as a function of the excitation frequency ν_1 and detection frequency ν_3 are gained by 2D Fourier transforms.

among the different contributions which is required for signal processing is automatically fulfilled.

In Figure 3, we present the results of model calculations for an inhomogeneous ensemble of two-level systems driven by two δ -like pulses A and B. The six contour plots show the nonlinearly emitted electric field as a function of t and τ . The columns 2–4 of Table 1 show that the various contributions to the third-order nonlinear signal differ either in time ordering of pulses A and B (i.e., $\tau > 0$ or $\tau < 0$) or in the direction of the frequency vector $\vec{\nu} = (\nu_B, \nu_A)$ (black arrows in Figure 3). Three types of experiments are distinguished, i.e., (a, f) photon echo, (b, d) pump–probe, and (c, e) the so-called perturbed free induction decay (PFID) of the respective pump–probe experiment (probe precedes pump).

If the pulses A and B were identical, i.e., $\nu_A = \nu_B = \nu_0$, the pairs of measurements (a,f), (b,d), and (c,e) would give identical information. The experimental scheme, however, allows for using pulses A and B with different center frequencies ν_A and ν_B as shown in Figure 5(b). In such a case, the six experiments of Figure 3 and Table 1 give different results and, thus, complementary information on the nonlinear response function.

We now discuss how to derive the 2D correlation spectrum from time-resolved data recorded in a collinear interaction geometry. The 2D spectrum is a function of the excitation frequency ν_1 and detection frequency ν_3 , the Fourier conjugates of τ_{ex} and t_{det} in the interaction sequence of Figure 1. The absorptive 2D spectrum is given by the sum of the rephasing and nonrephasing third-order signals, requiring a so-called phasing procedure in the processing of the data.⁷ In the collinear scheme, the phasing procedure is equivalent to a simple time reordering of the different experiments of Figure 3 according to Table 1. As a result, one gets a 2D correlation spectrum with purely absorptive line shapes as visualized in Figure 4. For instance, the A–B–B photon echo of Figure 3(a) is a rephasing contribution. Its nonrephasing counterpart is the ($\tau \leftrightarrow -\tau$)-inverted perturbed free induction decay of the B pump–A probe experiment (Figure 4b). Panel (c) shows the sum of the rephasing and nonrephasing contributions. The corresponding 2D correlation spectra as a function of the excitation

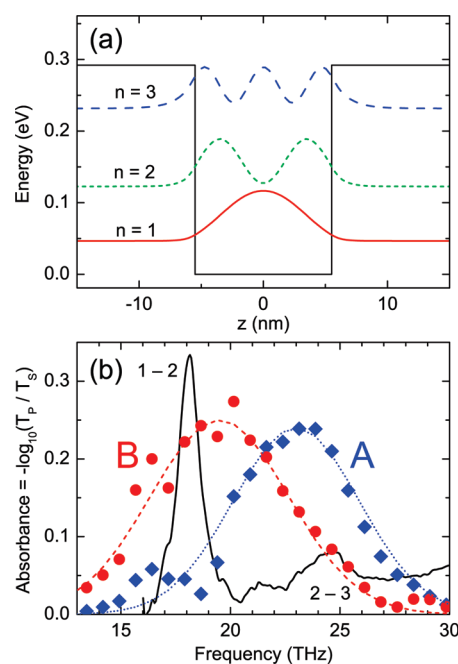


Figure 5. (a) Potential energy and $|\Psi_n(x)|^2$ for the three lowest subbands of an AlGaAs/GaAs quantum well of 11 nm width. (b) Black solid line: linear intersubband absorption at room temperature. The two absorption lines correspond to the $1 \leftrightarrow 2$ and $2 \leftrightarrow 3$ transitions between bound states in the quantum well. Symbols: measured spectra of the transmitted THz pulses A (diamonds) and B (circles). Dashed and dotted lines: Gaussian fits to the measured pulse spectra.

frequency ν_1 and detection frequency ν_3 (lower row of Figure 4) are calculated by a two-dimensional Fourier transform, giving the absorptive 2D spectrum in Figure 4(f). The procedure described here consists essentially of time-ordering all measured nonlinear signals to a $S(\tau_{\text{ex}} T_W t_{\text{det}})$ sequence before summing them up coherently to generate the total third-order nonlinear response function.

A comment should be made on the validity of the formalism applied so far (and in ref 7) to derive 2D spectra. The calculations are based on a perturbative density matrix approach in rotating wave approximation, i.e., neglect nonresonant contributions. Moreover, contributions from multiple interactions of a single pulse during temporal pulse overlap are neglected. To assess such assumptions, we performed density matrix calculations without rotating wave approximation.³⁶ One important result is the fact that nonresonant terms and multiple interactions can be neglected only when the relation $\omega_{\text{system}} \gg \Delta\omega_{\text{pulse}} \gg \Delta\omega_{\text{system}}$ holds (ω_{system} , transition frequency; $\Delta\omega_{\text{pulse}}$, spectral bandwidth of the pulses; $\Delta\omega_{\text{system}}$, spectral width of the transition). For the experiments discussed in ref 7, one estimates a ratio of $\omega_{\text{system}} : \Delta\omega_{\text{pulse}} : \Delta\omega_{\text{system}} = 30:3:1$, whereas a typical experiment in the THz range has a ratio of only $\omega_{\text{system}} : \Delta\omega_{\text{pulse}} : \Delta\omega_{\text{system}} = 4:2:1$. For shorter THz pulses (larger $\Delta\omega_{\text{pulse}}$), nonresonant interaction terms come into play. For longer pulses of high intensity, one has to consider multiple interactions of one pulse with the system during the pulse overlap. A general advantage of the density matrix approach is that it is not restricted to the $\chi^{(3)}$ limit and, thus, can describe phenomena like Rabi oscillations.^{32,36}

3. EXPERIMENTAL RESULTS AND DISCUSSION

We now present experimental results on a prototype semiconductor quantum well sample to illustrate the potential of

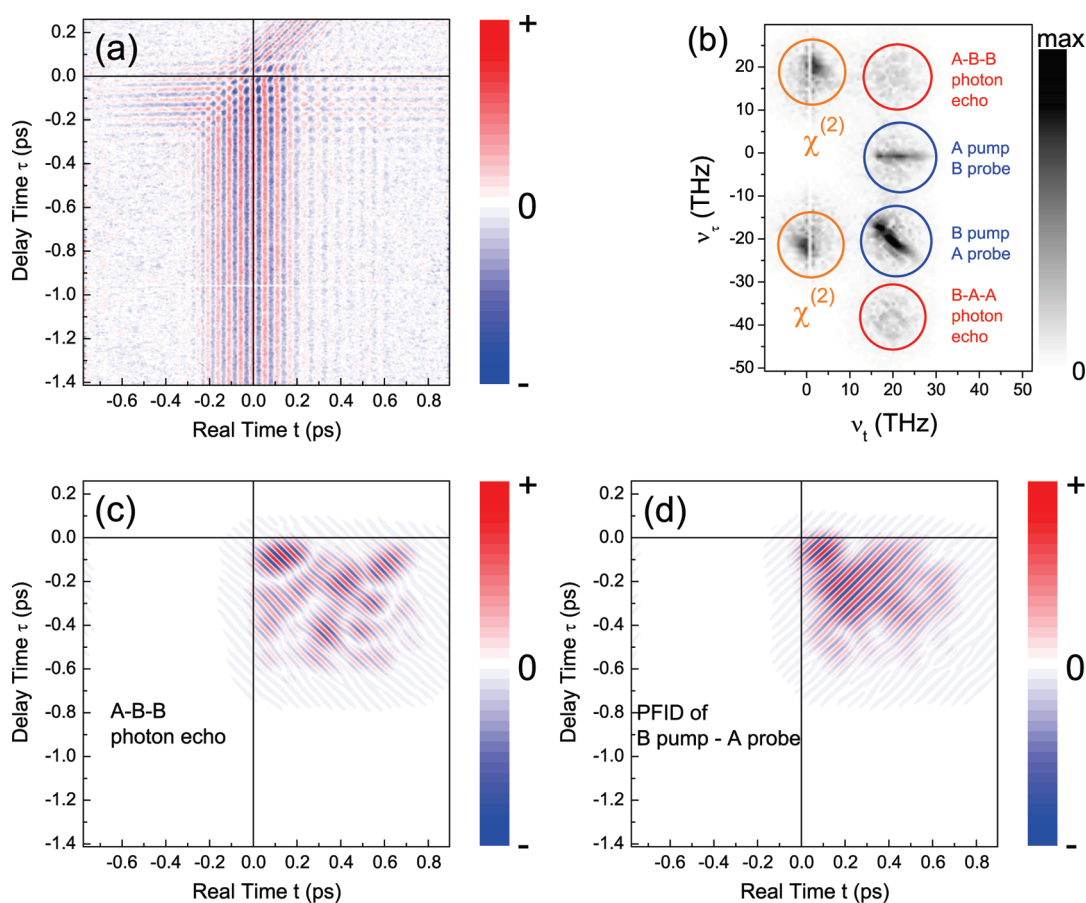


Figure 6. (a) Emitted nonlinear signal as a function of real time t and delay time τ . (b) The corresponding two-dimensional (amplitude) spectrum exhibits two pump–probe signals (pump A–probe B and vice versa), two photon-echo peaks, and difference-frequency mixing contributions, i.e., $\chi^{(2)}$ contributions. (c) A–B–B photon-echo contribution to the nonlinear signal (rephasing signal). (d) Perturbed free induction decay contribution of the B pump–A probe experiment (nonrephasing signal).

collinear 2D THz spectroscopy. The prism-shaped sample consists of 20 GaAs quantum wells of 11 nm width (Figure 5a). The quantum wells are separated by 20-nm-thick $\text{Al}_{0.35}\text{Ga}_{0.65}\text{As}$ barriers, the centers of which are doped with Si, resulting in an electron concentration of $n_s = 1.5 \times 10^{11} \text{ cm}^{-2}$ per quantum well. According to a $k \cdot p$ calculation, the sample has bound states at 50 meV ($n = 1$), 120 meV ($n = 2$), and 230 meV ($n = 3$) (Figure 5a). Two intersubband transitions of electrons $1 \leftrightarrow 2$ at 18 THz and $2 \leftrightarrow 3$ at 25 THz are observed in linear absorption (Figure 5b). While the dipole moments on the $1 \leftrightarrow 2$ and $2 \leftrightarrow 3$ transition are of similar magnitude, the small thermal population of the $n = 2$ subband $n_2 \approx 0.05n_1$ results in a much weaker $2 \leftrightarrow 3$ absorption.

The experimental setup for collinear 2D spectroscopy has been described in detail in ref 32. In brief, the output of a femtosecond Ti:sapphire multipass amplifier (repetition rate 1 kHz) is split and sent into two GaSe crystals to generate two phase-locked pulses A and B by difference frequency mixing.³⁸ The temporal position of pulse B is kept fixed, while pulse A and, thus, the delay τ is varied after each scan along the real time t . The center frequencies of the pulses A (diamonds in Figure 5b) and B (circles in Figure 5b) are set to match the observed intersubband transitions (black solid line in Figure 5b). The electric field amplitudes of pulses A and B are in a range between 50 and 100 kV/cm. Two choppers synchronized to the amplifier repetition rate allow for measuring the transients $E_{AB}(t, \tau)$

(both pulses A and B are incident on the sample), $E_A(t, \tau)$ (only pulse A), and $E_B(t)$ (only pulse B).

The nonlinear signal which is emitted by the sample and obtained as the difference $E_{NL}(t, \tau) = E_{AB}(t, \tau) - E_A(t, \tau) - E_B(t)$ is shown as a two-dimensional contour plot in Figure 6. Panel (a) shows the electric field emitted by the total nonlinear polarization as a function of real time t and delay time τ . A subsequent Fourier transformation provides the corresponding two-dimensional (amplitude) spectrum which is plotted as a function of ν_t and ν_τ in panel (b). It exhibits two pump–probe signals (pump A–probe B and vice versa), two photon-echo peaks, and two peaks caused by the $\chi^{(2)}$ -effect of the sample. The latter difference-frequency mixing contributions do not stem from the quantum wells but from the bulk GaAs substrate of the prism-shaped sample and, thus, are not considered in the following. In Figure 6(c), the A–B–B photon-echo contribution is plotted as a function of t and τ , as derived by a Fourier back-transform of the A–B–B signal in panel (b). Its nonrephasing counterpart, i.e., the perturbed free induction decay contribution of the B pump–A probe experiment, is shown in Figure 6(d).

Applying the procedure discussed in section 2.2 to the data in Figure 6(c,d), we obtain the (absorptive) 2D correlation spectrum shown in Figure 7(a) which is a contour plot as a function of the excitation frequency ν_1 and detection frequency ν_3 . Along the diagonal, we observe two pronounced positive peaks at 17.3 and 19.7 THz located on both sides of the $1 \leftrightarrow 2$ peak in the linear

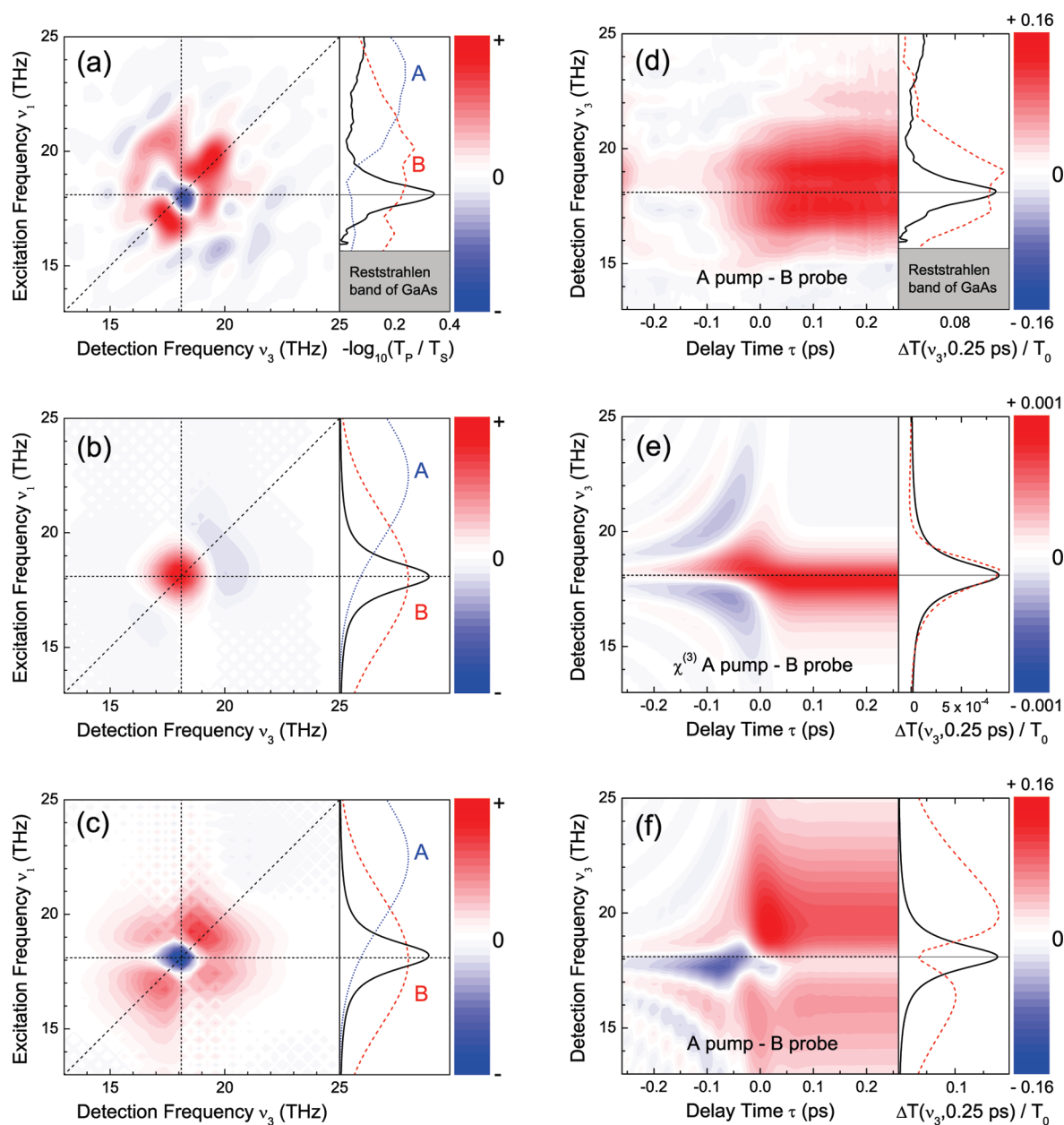


Figure 7. (a) 2D correlation spectrum (absorptive spectrum) as a function of the excitation frequency ν_1 and detection frequency ν_3 obtained from the measured 2D scan shown in Figure 6. The linear absorption spectrum and pulse spectra are shown for comparison on the right-hand side. (b) Calculated 2D correlation spectrum for a homogeneously broadened two-level system driven by weak pulses, i.e., in the $\chi^{(3)}$ limit. (c) Same two-level system driven by strong pulses. Applying the off-resonant pulse A plus the resonant pulse B with a pulse area of $\Theta_A + \Theta_B = 2\pi$ results in a complete Rabi flop of the two-level system. (d,e,f) Experimental and calculated signals of the corresponding A pump–B probe experiment. Here, the spectrally resolved transmission change $\Delta T(\nu_3, \tau)/T_0(\nu_3, -\infty)$ is plotted as a function of delay τ (contour plots). Panels on the right-hand side: Linear absorption spectrum (black lines) and cross section of the pump–probe signal for $\tau = 0.25$ ps (red dashed lines).

absorption spectrum (Figure 5). A 2D correlation spectrum shows signals along the excitation axis ν_1 exclusively at those positions where the sample absorbs light. On the right-hand side of Figure 7(a), we plot the linear absorption spectrum for comparison. It should be noted that there is no pronounced diagonal contribution to the 2D spectrum at the spectral position of the $2 \leftrightarrow 3$ intersubband transition at 25 THz, even though pulses A and B have significant spectral density at that spectral position (Figure 5b).

In addition to the 2D spectrum, we extracted the A pump–B probe signal from Figure 6(b) and calculated the spectrally

resolved transmission change according to

$$\frac{\Delta T(\nu_3, \tau)}{T_0(\nu_3, -\infty)} = \frac{E_{\text{NL}}^*(\nu_3, \tau)E_{\text{B}}(\nu_3) + E_{\text{NL}}(\nu_3, \tau)E_{\text{B}}(\nu_3)^*}{E_{\text{B}}(\nu_3)^*E_{\text{B}}(\nu_3)} \quad (5)$$

The result presented in Figure 7(d) does not display a pronounced signal on the $2 \leftrightarrow 3$ intersubband transition ($\nu_3 = 25$ THz) either. Evidently, the nonlinear response of our sample is dominated by the much stronger $1 \leftrightarrow 2$ intersubband transition at $\nu_3 = 18$ THz. The A pump–B probe signal in Figure 7(d) shows an unexpectedly broad spectral width on the $1 \leftrightarrow 2$

transition (red dashed line rhs of Figure 7(d)) which is observed even at late times until the complete decay of the pump–probe signal (not shown).

A most interesting and surprising feature in the measured 2D correlation spectrum (Figure 7 a) is the intense negative signal (blue spot) on the diagonal located exactly at the absorption maximum of the $1 \leftrightarrow 2$ intersubband transition at 18 THz. Negative signals on the diagonal are absent in most published 2D spectra. To find out which mechanism can cause negative signals on the diagonal for $T_W = 0$, we performed model calculations based on the density matrix formalism without rotating wave approximation.³⁶ This approach is not restricted to the $\chi^{(3)}$ limit, and thus, we can investigate phenomena like Rabi oscillations.³²

In Figure 7(b,c) and (e,f) we show 2D correlation spectra and A pump–B probe signals, respectively, calculated for a homogeneously broadened two-level system with parameters close to the $1 \leftrightarrow 2$ intersubband transition of our sample. Panels (b) and (e) display results for the $\chi^{(3)}$ limit, i.e., an interaction of the sample with weak pulses. We get the expected result for the 2D correlation spectrum, a strong positive peak on the diagonal centered at 18 THz. Its shape is quite round and complemented by small negative signals in its vicinity. The latter features are a consequence of the small ratio $\omega_{\text{system}}:\Delta\omega_{\text{pulse}}:\Delta\omega_{\text{system}} = 4:2:1$ for our experimental situation (cf. section 2.2). The pump–probe signal calculated in the $\chi^{(3)}$ limit (Figure 7e) displays a perturbed free induction decay at negative delay times and matches at late delay times τ the spectral shape of the linear absorption spectrum almost perfectly. Both the sign of the calculated 2D correlation signal on the diagonal and the spectrum of the pump–probe signal at late delay times are in disagreement with the data in Figure 7(a,d). We conclude that the measured nonlinear response is beyond the $\chi^{(3)}$ limit.

A prominent mechanism generating a strong negative signal on the diagonal is the interaction of a sequence of strong pulses with the two-level system. Calculations for this limit are shown in Figure 7(c) and (f). We characterize the strength of the pulses by their pulse area given by

$$\Theta_{A,B} = \frac{d_{12}}{\hbar} \int_{-\infty}^{+\infty} \mathcal{R}[\varepsilon_{A,B}(t)] dt \quad (6)$$

d_{12} is the transition dipole moment; \hbar is Planck's constant divided by 2π ; and $\mathcal{R}[\varepsilon_{A,B}(t)]$ is the real part of the slowly varying envelope of the pulses. (Please note that the relation $\Theta = \int \Omega_{\text{Rabi}} dt$ is not strictly fulfilled for nonresonant interactions beyond the rotating wave approximation.) According to the reduced spectral overlap with the intersubband absorption line, an off-resonant pulse has a smaller area than a resonant one, i.e., $\Theta_A \approx 0.5\Theta_B$.

In the particular case shown in Figure 7(c) and (f), the application of the off-resonant pulse A plus the resonant pulse B with a total pulse area $\Theta_A + \Theta_B = 2\pi$ results in a complete Rabi flop of the two-level system. The complete inversion of the system by the first pulse leads to stimulated emission triggered by the second pulse and a π phase change of the nonlinearly emitted electric field (negative signal on the diagonal in Figure 7c). An analysis of the pump–probe part of our calculation (Figure 7f) shows that the Rabi flopping during the pulse overlap causes—at late delay times τ —a pronounced minimum of the A pump–B probe signal at the peak position of the linear absorption spectrum. We see a precursor of this theoretically predicted dip in our experimental data (red dashed line rhs of Figure 7d).

On the basis of the strong resemblance of Figure 7(a) with panel (c) and of Figure 7(d) with panel (f), we assign the negative peak on the diagonal of the 2D spectrum and the spectral envelope of the pump–probe signal at late delays to a 2π Rabi flop. The extremely large dipole moment of the intersubband transition $d \approx e_0 \times 2.5 \text{ nm}$ (e_0 : elementary charge) leads to a very strong coupling to the THz field with the result that a 100 fs long resonant THz pulse with an amplitude of 50 kV/cm is already a π -pulse. Thus, even nonresonantly driving THz pulses with amplitudes of several tens of kilovolts per centimeter can be used for quantum control in collinear 2D terahertz spectroscopy similar to the well-developed concepts in NMR.³³

4. CONCLUSIONS

In conclusion, we have demonstrated the measurement of two-dimensional correlation spectra in the THz domain. In a collinear interaction geometry of phase-locked pulse sequences with a semiconductor quantum well sample, different contributions to the nonlinear intersubband response of electrons were separated and analyzed by calculations beyond the rotating-wave approximation. The shape of the 2D correlation spectrum and the spectrum of the pump–probe signal display features due to a Rabi flop induced by THz pulses of moderate electric field strength. The strong coupling of the large intersubband dipoles to the THz field will allow for implementing coherent control schemes to steer the response of the system, very similar to the concepts applied in nuclear magnetic resonance. Moreover, collinear 2D THz spectroscopy has the potential to unravel complex coupling schemes of elementary excitations in bulk and nanostructured solids. Work along those lines is presently underway.

AUTHOR INFORMATION

Corresponding Author

*E-mail: woerner@mbi-berlin.de.

REFERENCES

- (1) Mukamel, S. *Annu. Rev. Phys. Chem.* **2000**, *51*, 691.
- (2) Hamm, P.; Lim, M.; Hochstrasser, R. M. *J. Phys. Chem. B* **1998**, *102*, 6123.
- (3) Asplund, M. C.; Zanni, M. T.; Hochstrasser, R. M. *Proc. Natl. Acad. Sci. U.S.A.* **2000**, *97*, 8219.
- (4) Okumura, K.; Tokmakoff, A.; Tanimura, Y. *Chem. Phys. Lett.* **1999**, *314*, 488.
- (5) Woutersen, S.; Hamm, P. *J. Phys. Condens. Matter* **2002**, *14*, R1035.
- (6) Jonas, D. M. *Annu. Rev. Phys. Chem.* **2003**, *54*, 425.
- (7) Khalil, M.; Demirdöven, N.; Tokmakoff, A. *J. Phys. Chem. A* **2003**, *107*, 5258.
- (8) Cho, M.; Fleming, G. R. *J. Chem. Phys.* **2005**, *123*, 114506.
- (9) Cowan, M. L.; Bruner, B. D.; Huse, N.; Dwyer, J. R.; Chugh, B.; Nibbering, E. T. J.; Elsaesser, T.; Miller, R. J. D. *Nature* **2005**, *434*, 199.
- (10) Huse, N.; Bruner, B. D.; Cowan, M. L.; Dreyer, J.; Nibbering, E. T. J.; Miller, R. J. D.; Elsaesser, T. *Phys. Rev. Lett.* **2005**, *95*, 147402.
- (11) Hybl, J. D.; Yu, A.; Farrow, D. A.; Jonas, D. M. *J. Phys. Chem. A* **2002**, *106*, 7651.
- (12) Milota, F.; Sperling, J.; Nemeth, A.; Mancal, T.; Kauffmann, H. F. *Acc. Chem. Res.* **2009**, *42*, 1364.
- (13) Sperling, J.; Nemeth, A.; Hauer, J.; Abramavicius, D.; Mukamel, S.; Kauffmann, H. F.; Milota, F. *J. Phys. Chem. A* **2010**, *114*, 8179.
- (14) Brixner, T.; Stenger, J.; Vaswani, H. M.; Cho, M.; Blankenship, R. E.; Fleming, G. R. *Nature* **2005**, *434*, 625.

- (15) Cheng, Y. C.; Fleming, G. R. *Annu. Rev. Phys. Chem.* **2009**, *60*, 241.
- (16) Panitchayangkoon, G.; Hayes, D.; Fransted, K. A.; Caram, J. R.; Harel, E.; Wen, J. Z.; Blankenship, R. E.; Engel, G. S. *Proc. Natl. Acad. Sci. U.S.A.* **2010**, *107*, 12766.
- (17) Li, X. Q.; Zhang, T. H.; Borca, C. N.; Cundiff, S. T. *Phys. Rev. Lett.* **2006**, *96*, No. 057406.
- (18) Stone, K. W.; Gundogdu, K.; Turner, D. B.; Li, X. Q.; Cundiff, S. T.; Nelson, K. A. *Science* **2009**, *324*, 1169.
- (19) Turner, D. B.; Nelson, K. A. *Nature* **2010**, *466*, 1089.
- (20) Fecko, C. J.; Eaves, J. D.; Loparo, J. J.; Tokmakoff, A.; Geissler, P. L. *Science* **2003**, *301*, 1698.
- (21) Asbury, J. B.; Steinell, T.; Stromberg, C.; Corcelli, S. A.; Lawrence, C. P.; Skinner, J. L.; Fayer, M. D. *J. Phys. Chem. A* **2004**, *108*, 1107.
- (22) Eaves, J. D.; Loparo, J. J.; Fecko, C. J.; Roberts, S. T.; Tokmakoff, A.; Geissler, P. L. *Proc. Natl. Acad. Sci. U.S.A.* **2005**, *102*, 13019.
- (23) Kraemer, D.; Cowan, M. L.; Paarmann, A.; Huse, N.; Nibbering, E. T. J.; Elsaesser, T.; Miller, R. J. D. *Proc. Natl. Acad. Sci. U.S.A.* **2008**, *105*, 437.
- (24) Paarmann, A.; Hayashi, S.; Mukamel, S.; Miller, R. J. D. *J. Chem. Phys.* **2008**, *128*, 191103.
- (25) Bakulin, A. A.; Liang, C.; Jansen, T. L.; Wiersma, D. A.; Bakker, H. J.; Pshenichnikov, M. S. *Acc. Chem. Res.* **2009**, *42*, 1229.
- (26) Krummel, A. T.; Zanni, M. T. *J. Phys. Chem. B* **2006**, *110*, 13991.
- (27) Zheng, J. R.; Kwak, K.; Asbury, J.; Chen, X.; Piletic, I. R.; Fayer, M. D. *Science* **2005**, *309*, 1338.
- (28) Manor, J.; Mukherjee, P.; Lin, Y. S.; Leonov, H.; Skinner, J. L.; Zanni, M. T.; Arkin, I. T. *Structure* **2009**, *17*, 247.
- (29) Cervetto, V.; Helbing, J.; Bredenbeck, J.; Hamm, P. *J. Chem. Phys.* **2004**, *121*, 5935.
- (30) Yang, L.; Zhang, T.; Bristow, A. D.; Cundiff, S. T.; Mukamel, S. *J. Chem. Phys.* **2008**, *129*, 234711.
- (31) Tian, P.; Keusters, D.; Suzuki, Y.; Warren, W. S. *Science* **2003**, *300*, 1553.
- (32) Kuehn, W.; Reimann, K.; Woerner, M.; Elsaesser, T. *J. Chem. Phys.* **2009**, *130*, 164503.
- (33) Ernst, R. R.; Bodenhausen, G.; Wokaun, A. *Principles of Nuclear Magnetic Resonance in One and Two Dimensions*; Oxford University Press: Oxford, 1987.
- (34) Bristow, A. D.; Karauskaj, D.; Dai, X.; Cundiff, S. T. *Opt. Express* **2008**, *16*, 18017.
- (35) Backus, E. H. G.; Garrett-Roe, S.; Hamm, P. *Opt. Lett.* **2008**, *33*, 2665.
- (36) Luo, C. W.; Reimann, K.; Woerner, M.; Elsaesser, T.; Hey, R.; Ploog, K. H. *Phys. Rev. Lett.* **2004**, *92*, 047402.
- (37) Kaundl, R. A.; Wurm, M.; Reimann, K.; Hamm, P.; Weiner, A. M.; Woerner, M. *J. Opt. Soc. Am. B* **2000**, *17*, 2086.
- (38) Reimann, K.; Smith, R. P.; Weiner, A. M.; Elsaesser, T.; Woerner, M. *Opt. Lett.* **2003**, *28*, 471.